Understanding changes in ENSO variability over the Holocene

Steven J. Phipps

CSIRO Marine and Atmospheric Research, Aspendale, Victoria, Australia (steven.phipps@csiro.au)
Centre for Australian Weather and Climate Research, Aspendale, Victoria, Australia

1. Introduction

Proxy reconstructions from across the Pacific Basin (e.g. Rodbell et al., 1999) indicate that significant changes in ENSO characteristics took place during the Holocene. “Modern” El Niño variability began around 7–5 ka BP, with only weak decadal-scale events occurring beforehand. ENSO was 15–60% weaker at 6 ka than at present, with a gradual strengthening thereafter. There is also evidence of a peak in strength at 2–1 ka.

The coupled models participating in PMIP2 simulate El Niño amplitudes that are 2.9–23% weaker at 6 ka than at present (Zheng et al., 2008), with a consistent mechanism found to apply across all the models. Insolation changes during the mid-Holocene result in an enhanced seasonal cycle in the Northern Hemisphere, leading to an intensification of the summer monsoon system. This enhances the strength of the easterly trade winds in the central and western Pacific, causing increased upwelling in the central and eastern Pacific and hence suppressing the development of El Niño events.

Here, we use a coupled model to simulate the orbitally-driven changes in the climate over the past 10,000 years. The simulations are then used to investigate the role of orbital forcing in driving changes in ENSO variability, as well as to investigate the underlying mechanisms.

2. Experiments

We use the CSIRO Mk3L climate system model v1.1 (Phipps, 2006). This model has participated in PMIP2, taking part in the 0K_OA and 6K_OA experiments. It comprises atmospheric and oceanic general circulation models with resolutions of R21 18L and 2.8°×1.6° 21L respectively, a dynamic-thermodynamic sea ice model, and a land surface scheme with static vegetation.

Equilibrium simulations are conducted for 10, 9, 8, 7, 6, 5, 4, 3, 2, 1 and 0 ka BP. These are idealised experiments, in that *only* the Earth’s orbital parameters are varied. Otherwise, the model is configured exactly as for the PMIP2 0K_OA experiment, with an atmospheric CO_2 concentration of 280 ppm and a solar constant of 1365 Wm^{-2}. No changes are made to either the ice sheets or the topography, and it should therefore be emphasised that the 10 and 9 ka simulations are significantly unrepresentative of the true conditions that prevailed at these times.

Each experiment is integrated for 1000 years under constant boundary conditions. Flux adjustments are employed, ensuring a reference state that is in good agreement with observations. Figure 1 shows the simulated SSTs for 0 ka, as well as the leading EOF of the monthly SST anomalies. Peak ENSO variability can be seen to occur within the Niño 3.4 region.

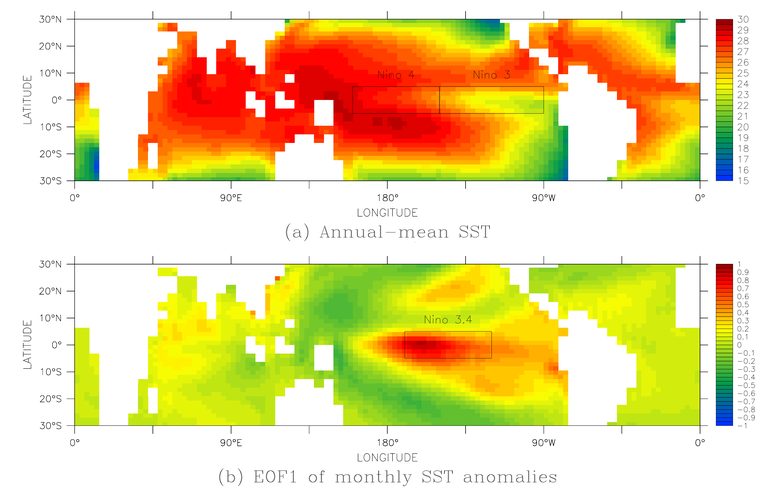

(a) Annual−mean SST

(b) EOF1 of monthly SST anomalies

Figure 1. Simulated sea surface temperatures for 0 ka: **a** the annual mean (°C), and **b** the leading EOF of the monthly anomalies (°C). Also shown are the Niño 3, Niño 3.4 and Niño 4 regions.

3. Changes in the mean state

Figure 2 shows the simulated evolution of the mean state of the tropical Pacific. In response to increasing tropical insolation during the Holocene, the annual-mean SST increases in both the eastern and western Pacific. The zonal SST gradient, as given by the difference between the Niño 3 and Niño 4 SSTs, increases after 5 ka; this is associated with a decrease in the strength of the easterly trade winds. However, it should be noted that the magnitude of all these changes is small.

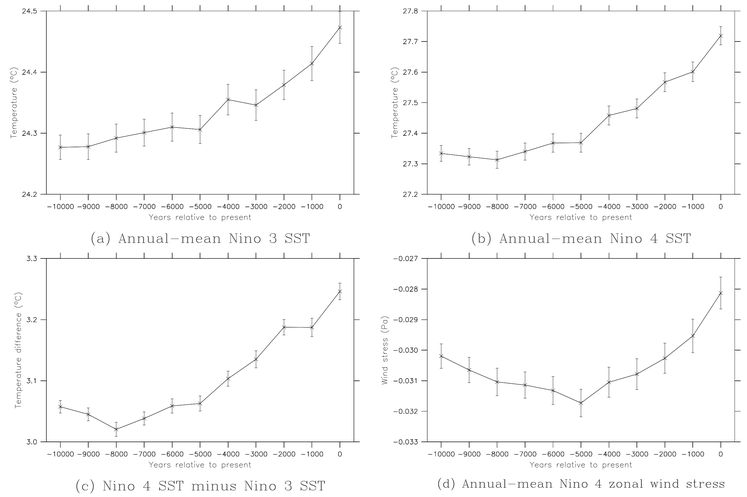

(a) Annual−mean Nino 3 SST

(b) Annual−mean Nino 4 SST

(c) Nino 4 SST minus Nino 3 SST

(d) Annual−mean Nino 4 zonal wind stress

Figure 2. The mean state of the tropical Pacific: **a** and **b** the annual-mean SST in the Niño 3 and Niño 4 regions, **c** the difference between the annual-mean Niño 3 and Niño 4 SSTs, and **d** the annual-mean zonal wind stress in the Niño 4 region. The 95% confidence intervals are shown.

4. Changes in ENSO variability

Figure 3a shows the standard deviations of the simulated Niño 3 and Niño 3.4 SST anomalies. The model captures the observed changes well, with an increase in ENSO variability during the Holocene and a statistically-significant peak in strength at 1 ka.

Based on the Niño 3 SST anomalies, the amplitude of El Niño is 13% weaker at 6 ka than at present; based on the Niño 3.4 SST anomalies, it is 16% weaker. This is consistent with the other PMIP2 models, but at the upper limit of the reconstructed uncertainty range. At 10 ka, El Niño is 23% (Niño 3) and 27% (Niño 3.4) weaker than at present.

Consistent with the mechanism of Zheng et al. (2008), the easterly trade winds weaken throughout the mid- and late Holocene (Figure 3b). However, changes in the trade winds do not explain the peak in ENSO variability at 1 ka; neither is there any correlation between the strength of the trade winds and the strength of ENSO during the early Holocene.

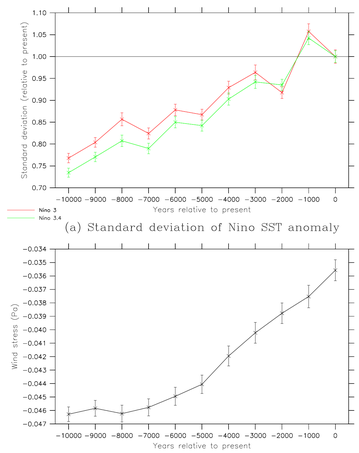

(a) Standard deviation of Nino SST anomaly

(b) JASO zonal wind stress in Nino 4 region

Figure 3. **a** The normalised standard deviations of the Niño 3 and Niño 3.4 SST anomalies, and **b** the July–August–September–October zonal wind stress in the Niño 4 region. The 95% confidence intervals are shown.

We now apply some of the diagnostics developed by Guilyardi (2006). Figure 4a shows the seasonal phase lock, which is defined as the annual amplitude of the monthly stratified standard deviation of the Niño 3 SST anomaly. After 5 ka, there is an upward trend in the SPL. This indicates an increasing seasonal relaxation of the easterly trade winds, which allows El Niño events to arise more readily. The strongest phase lock occurs at 1 ka, indicating that seasonal changes can explain the peak in ENSO variability at this time.

Figure 4b shows the “summer” (June–November) interannual coupling strength. The ICS is defined as the slope of the linear fit of the Niño 4 wind stress anomalies to the Niño 3 SST anomalies, and represents a measure of the atmospheric response to changes in the surface ocean. There is an upward trend in the ICS during the Holocene, indicating an increase in the strength of the atmosphere-ocean coupling. The stronger coupling gives rise to an increase in the strength of ENSO.

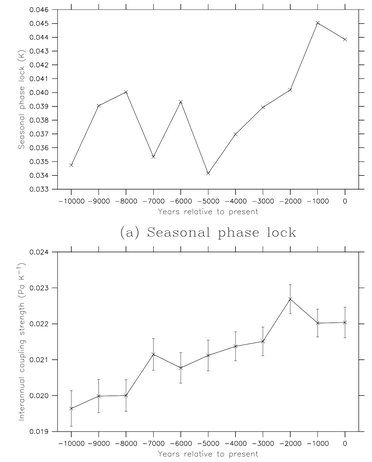

(a) Seasonal phase lock

(b) Summer interannual coupling strength

Figure 4. **a** The seasonal phase lock, and **b** the “summer” (June–November) interannual coupling strength. The 95% confidence interval is shown in **b**.

5. Conclusions

A coupled atmosphere-ocean general circulation model has been forced with orbitally-driven insolation changes. It is able to reproduce the reconstructed changes in ENSO variability over the Holocene, although the magnitude of the simulated changes may be too small.

The mean state of the tropical Pacific is almost invariant, indicating that changes in ENSO characteristics are driven by changes in the seasonal cycle. The mechanism identified by Zheng et al. (2008) - whereby an enhanced seasonal cycle in the Northern Hemisphere drives changes in ENSO via the summer monsoon system and the easterly trade winds - appears to explain the gradual increase in ENSO variability throughout the mid- and late Holocene. However, it does not explain the peak at 1 ka, nor the changes during the early Holocene. Other mechanisms are clearly therefore at work.

A full understanding of the processes that drive changes in ENSO variability may be within grasp. However, this will require an approach that integrates the theory, data and modelling communities.

6. References

Guilyardi, E. (2006), El Niño–mean state–seasonal cycle interactions in a multi-model ensemble, *Climate Dynamics*, *26*, 329–348.

Phipps, S. J. (2006), The CSIRO Mk3L Climate System Model, *Technical Report No. 3*, Antarctic Climate & Ecosystems Cooperative Research Centre, Hobart, Tasmania, Australia, 236 pp., ISBN 1-921197-03-X.

Rodbell, D. T., G. O. Seltzer, D. M. Anderson, M. B. Abbott, D. B. Enfield and J. H. Newman (1999), An ∼15,000-Year Record of El Niño–Driven Alluviation in Southwestern Ecuador, *Science*, *283*, 516–520.

Zheng, W., P. Braconnot, E. Guilyardi, U. Merkel and Y. Yu (2008), ENSO at 6ka and 21ka from ocean-atmosphere coupled model simulations, *Climate Dynamics*, *30*, 745–762.

Acknowledgements: I would like to thank the ARC Research Network for Earth System Science, PMIP2 and CSIRO Marine and Atmospheric Research for travel support.